


## Article

# A Late Cambrian Continental Convergent Margin in the North Qilian Orogenic Belt, Northwestern China: Geochemical and Geochronological Evidence from Hongtugou Mafic Rocks

Jian Wang <sup>1,2</sup>, Gen Xie <sup>1,3</sup>, Guanghai Shi <sup>1,\*</sup>  and Jian Niu <sup>4</sup>

<sup>1</sup> State Key Laboratory of Geological Processes and Mineral Resources, China University of Geosciences, Beijing 100083, China

<sup>2</sup> School of Earth and Environmental Sciences, Cardiff University, Cardiff CF10 3AT, UK

<sup>3</sup> Langfang General Survey of Natural Resources Center, China Geological Survey, Langfang 065000, China

<sup>4</sup> Shanxi Institute of Geological Survey Co., Ltd., Taiyuan 030006, China

\* Correspondence: shigh@cugb.edu.cn; Tel.: +86-10-82321836

**Abstract:** The tectonic setting and subduction polarity of the early Paleozoic North Qilian Orogenic Belt (NQOB) in northwestern China is poorly constrained due to complex tectonic deformation. Mafic and ultramafic rocks in the South Ophiolite Belt of the NQOB are interpreted to be middle ocean ridge ophiolite or suprasubduction zone ophiolite. To address this, we have conducted geochemical and geochronological investigations of the mafic rock sequence (cumulate gabbros, diabases, isotropic gabbros, and basalts) in Hongtugou in the South Ophiolite Belt. Trace element characteristics of the pillow basalts and the isotropic gabbros with enrichment of Th and La relative to Nb on the N-MORB normalized multi-element diagram are consistent with a suprasubduction setting, where similarities with the Panamanian proto-arc rocks suggest they formed shortly after subduction initiation. Major element modelling for cumulate gabbros and basalts indicates the hydrous condition of crystallization which further supports a suprasubduction setting. The Proterozoic zircon crystals captured in a cumulate gabbro and a diabase suggest this suprasubduction zone is a continental convergent margin. A weighted mean zircon SHRIMP age of  $507 \pm 6$  Ma from an isotropic gabbro is consistent with crystallization ages of other mafic rocks in this belt. This suggests the North Qilian oceanic lithosphere subducted beneath the continent in the late Cambrian. Mafic rocks in this study along with the serpentinized peridotite do not fall into the category of ophiolite, despite displaying an ophiolite sequence.

**Keywords:** North Qilian; subduction initiation; continental convergent margin; ophiolite; late Cambrian



**Citation:** Wang, J.; Xie, G.; Shi, G.; Niu, J. A Late Cambrian Continental Convergent Margin in the North Qilian Orogenic Belt, Northwestern China: Geochemical and Geochronological Evidence from Hongtugou Mafic Rocks. *Minerals* **2022**, *12*, 1105. <https://doi.org/10.3390/min12091105>

Academic Editor: Jan C.M. De Hoog

Received: 29 June 2022

Accepted: 23 August 2022

Published: 30 August 2022

**Publisher's Note:** MDPI stays neutral with regard to jurisdictional claims in published maps and institutional affiliations.



**Copyright:** © 2022 by the authors. Licensee MDPI, Basel, Switzerland. This article is an open access article distributed under the terms and conditions of the Creative Commons Attribution (CC BY) license (<https://creativecommons.org/licenses/by/4.0/>).

## 1. Introduction

Orogenic belts can be divided into accretionary and collisional orogenic belts which can form at different stages of the “Wilson cycle” [1,2]. Ophiolites can provide insight into orogenic evolution since they are commonly found in orogenic belts. Initially, ophiolites were considered to represent the oceanic lithosphere formed in the middle ocean ridge until Miyashiro (1973) [3] proposed a suprasubduction origin for the Troodos ophiolite. Today, ophiolites are divided into subduction-related and subduction-unrelated [4], yet both types are considered as an allochthonous fragment of upper mantle (i.e., mantle peridotite) and oceanic crustal rocks (i.e., ultramafic to felsic crustal intrusive and volcanic rocks with or without sheeted dikes) that have been tectonically displaced due to plate convergence. This classification is based on improving the knowledge of seafloor spreading which can occur in several tectonic settings in addition to the middle ocean ridge [5]. On the contrary, ophiolites formed in middle ocean ridges (MOR ophiolites) are rare compared with other ophiolites (e.g., suprasubduction zone or SSZ ophiolites), as the vast majority of oceanic lithosphere subducts cannot be preserved [6]. For mantle peridotites, they

include lherzolite and harzburgite with lenses of dunite and chromitite usually showing high-temperature deformation fabrics [6]. Similar to the ophiolitic peridotite, orogenic peridotites are also common in orogenic belts and can also coexist with mafic rocks [7]. However, orogenic peridotites represent the subcontinental lithosphere mantle [7–9] and are generally associated with platform sediments or metamorphosed continental rocks [7].

Primitive magmatic rocks formed above subduction zones (e.g., volcanic arc basalts and boninite in subduction-related ophiolites) are usually enriched in fluid mobile elements (e.g., Rb, Ba, Pb), light rare earth elements, U, and Th due to metasomatism by slab components [10,11]. Without the addition of slab components, magmas in the middle ocean ridge formed due to decompression melting and do not show enrichment of these elements compared with Nb, Ta, and heavy rare earth elements. However, rocks formed in fore-arc basins shortly after subduction initiation such as the Izu-Bonin-Mariana fore-arc basalts (FAB) [12–14] and the Panamanian proto-arc rocks [15] only show weak arc signature. The mantle source is slightly affected by slab components and magmatism is mainly attributed to decompression melting due to fore-arc extension [12]. The chemical characteristics of the MOR and SSZ rocks can be overlapped. Therefore, identifying the tectonic settings is crucial to deciphering the tectonic evolution of orogenic belts.

Mafic and ultramafic rock sequence in the NQOB has been previously interpreted as ophiolite (see references in Song et al., 2013 [16]). However, whether it is ophiolite or not and what type of ophiolite (MOR vs SSZ) it is controversial [16–18]. Determining its tectonic setting is the key to understanding the tectonic evolution of NQOB and maybe the evolution of proto-Tethys. Therefore, we have conducted whole rock geochemistry and SHRIMP U-Pb zircon geochronology of mafic rocks in Hongtugou in NQOB to help constrain the tectonic-magmatic evolution of the NQOB. Our data suggests that these mafic rocks are formed in a continental convergent margin possibly shortly after subduction initiation.

## 2. Geological Background

The NQOB is a ~1000 km NW-SE trending orogenic belt in the northern margin of the Tibetan Plateau (Figure 1). It is bordered by the Alashan Block in the north and Qilian Block in the south. In the west, it is bordered by the Tarim Craton along the left-lateral Altyn fault, which has been offset by up to 400 km [19]. The Alashan Block consists predominantly of a 2.3–1.9 Ga tonalitic/granitic gneiss basement [20–22] and Cambrian to middle Ordovician cover sequences [16]. The Archean basement is signified by the ~2.7 Ga amphibolite in the northeast part of the block [22], as well as by some 2.5–3.5 Ga detrital zircons from meta-sedimentary sequences [23,24]. The late Proterozoic Jinchuan ultramafic intrusion together with the synchronous mafic dyke swarm in the southern part, has been suggested to be the product of a superplume that triggered the breakup of the supercontinent Rodinia [25]. The Qilian Block, with the North Qaidam ultra-high pressure metamorphic belt to its south, is an imbricate thrust belt of Precambrian basement consisting of granitic gneiss, marble, amphibolite and minor granulite [26,27], overlain by Paleozoic sedimentary sequences. Archean zircon grains have been discovered in gneiss and schist [28–30].

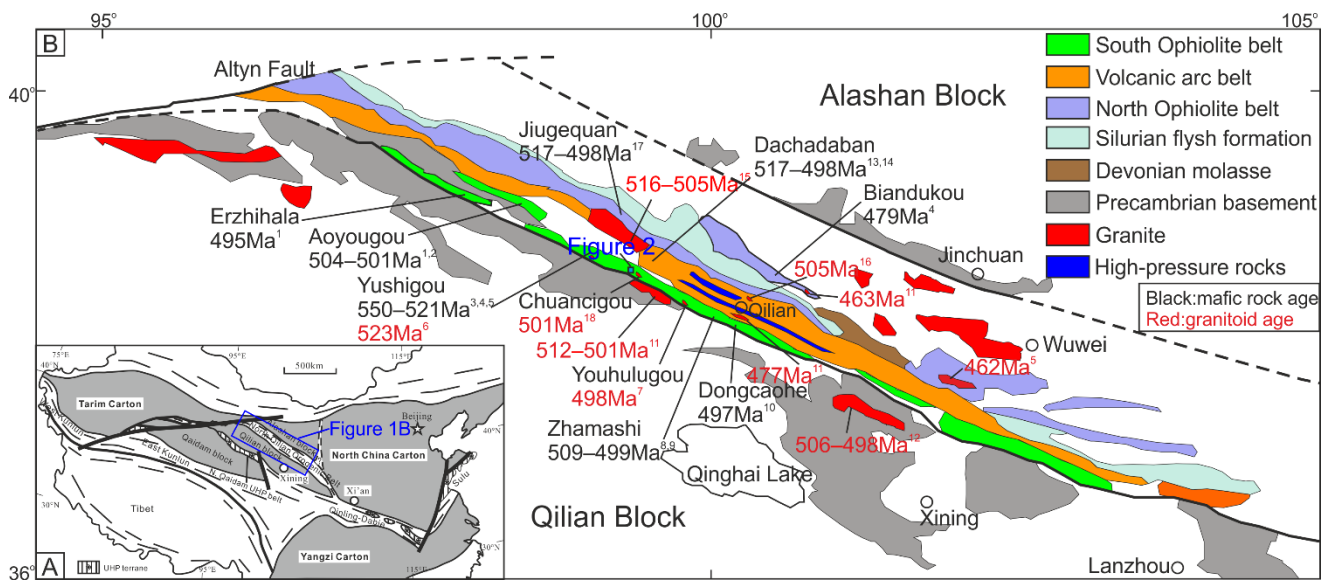


**Figure 1.** Geological map of the NQOB modified after Song et al. (2013) [16]. (A) is a schematic map showing major tectonic units of China and (B) is a geological map showing ages of the NQOB and Qilian Block. References: [31]<sup>1</sup>, [32]<sup>2</sup>, [33]<sup>3</sup>, [16]<sup>4</sup>, [18]<sup>5</sup>, [34]<sup>6</sup>, [35]<sup>7</sup>, [36]<sup>8</sup>, [37]<sup>9</sup>, [38]<sup>10</sup>, [39]<sup>11</sup>, [40]<sup>12</sup>, [41]<sup>13</sup>, [42]<sup>14</sup>, [43]<sup>15</sup>, [44]<sup>16</sup>, [45]<sup>17</sup>, [46]<sup>18</sup>.

The NQOB has been divided into three subunits by Song et al. (2013) [16]: the South Ophiolite Belt in the south, the North Ophiolite Belt in the north, and the continental arc belt in between. The North Ophiolite Belt is considered to form in a back-arc basin as this belt sits behind the continental arc belt and the mafic rocks show slab components [16,45,47]. The tectonic setting for the South Ophiolite Belt is controversial as some consider it as a MOR-type ophiolite [16,33,37,38] while others consider it to form in a supra-subduction zone [18,36]. The Qilian Ocean started to form in the NQOB after continental rifting in the Neoproterozoic (e.g., 600–580 Ma [48] or 710 Ma [16]), though some suggest that the Qilian Ocean located between the Qaidam Block and the Qilian Block and the NQOB was a continental back-arc initiating at ca. 710 Ma during Qilian Ocean northward subduction [49]. After subsequent oceanic spreading, subduction initiated at ca. 517 Ma [41] forming an infant arc. Continental arc magmatism lasted from 516 to 494 Ma [16,45,47] while the back-arc spreading occurred from 490 Ma to 448 Ma [16,43,45]. The Qilian Ocean closed at ca. 440 Ma following the arc-continent collision and then continent subduction occurred at ca. 440–420 Ma forming the blueschist belt [16]. The continuity between the Qilian orogen and the Qinling orogen based on the similar Silurian adakitic rocks in both belts has been suggested [50] and therefore the northward subduction in the early Paleozoic might extend to Qinling in the east.

### 3. Materials and Methods

Samples for whole-rock major and trace element analyses were first crushed and ultrasonically cleaned and handpicked to remove visible contamination. They were powdered to 200 mesh in an agate ring mill at the Hebei Institute of Regional Geology and Mineral Survey (HIRGMS) (Hebei, China). Two batches were analysed for whole rock geochemistry with the first batch at the HIRGMS and the second in Wuhan Sample Solution Analytical Technology Co., Ltd., Wuhan, China. For the first batch, major elements were measured by X-ray fluorescence (XRF) Axiosmax (Spectris, London, UK). Titration was used to measure Fe<sup>2+</sup>. Trace elements were measured by ICP-MS X-Serise2 (ThermoFisher, Waltham, MA, USA). The precision and accuracy are better than 5% for major elements and 10% for trace elements. For the second batch, Zsx Primus II wavelength dispersive XRF (Rigaku, Tokyo, Japan) was used for the analysis of major elements. The relative standard deviation (RSD)

is less than 2%. Trace element analyses of whole rock were conducted on Agilent 7700e ICP-MS (Agilent Technologies, Inc., Anta Clara, CA, USA). Measured concentrations were calibrated against the BCR-2, BHVO-2 and RGM-2 national standards. The accuracy of trace element analysis was better than 10%. Data can be found in Supplementary Table S1.

Zircon crystals were hand-picked under a binocular microscope following heavy liquids and magnetic separation at the HIRGMS. Grains were mounted in epoxy and polished to expose grain interiors. Zircon morphology and internal structure were examined under transmitted and reflected light microscope followed by cathodoluminescence (CL) imaging at the Beijing SHRIMP Centre (Beijing, China). U-Pb zircon dating was conducted at this institute using SHRIMP-II. The standard SL13 (572 Ma) was used to measure the content of U, Th, and Pb and the standard TEM (417 Ma, [51]) was used to carry out fractionation correction. Common Pb was calibrated by measured  $^{204}\text{Pb}$ . The detailed processes can be found in Williams (1998) [52]. The analyzing spot is 25  $\mu\text{m}$  and one TEM was calibrated at every 3–4 analyses. Weighted mean age calculation and concordia plot were conducted using Isoplot 4.15 [53]. When  $^{206}\text{Pb}/^{238}\text{U}$  is smaller than 800 Ma, the  $^{206}\text{Pb}/^{238}\text{U}$  dates were adopted otherwise the  $^{206}\text{Pb}/^{207}\text{Pb}$  were adopted. The data can be found in Supplementary Table S2.

## 4. Results

### 4.1. Field Observation and Petrography

The rocks are mainly divided into cumulate gabbros (13HC-025), diabases (13HC-015), isotropic gabbros (14HC-005), and pillow basalts (14HC-003) according to field (Figure 2), petrographic and geochemical characteristics.

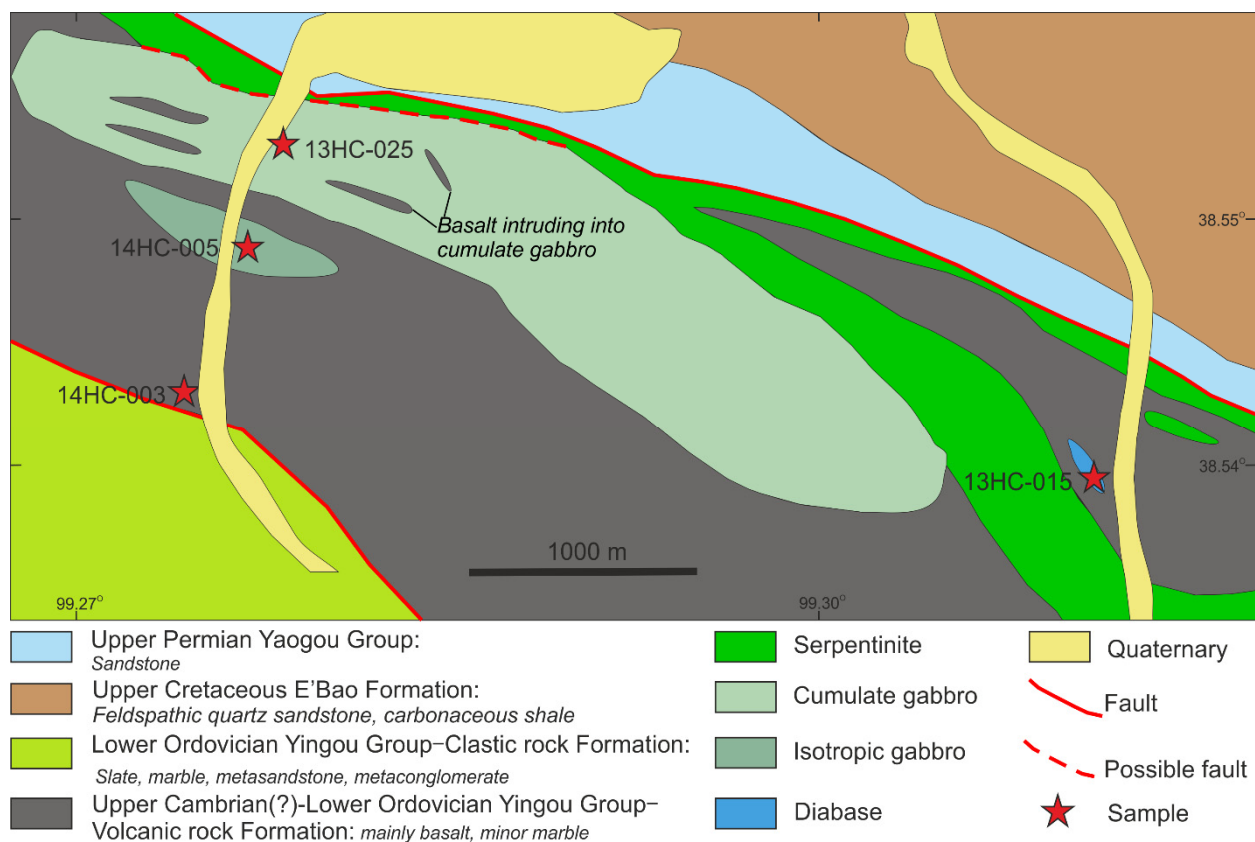


**Figure 2.** Geological map of Hongtugou. Modified after the map made by the No.6 Gold Geological Party of the Chinese Armed Police Force.

The cumulate gabbros mainly comprise cumulus plagioclase laths and anhedral, intercumulus clinopyroxene crystals (Figure 3A). Most of the plagioclase crystals have been replaced



by epidote due to metamorphism. The crystallization sequence is plagioclase-clinopyroxene. The diabases show (sub)ophitic texture with euhedral lath-shaped plagioclase crystals surrounded by anhedral and intercumulus clinopyroxene crystals (Figure 3B). The isotropic gabbros intruded into carbonate rock in the field (Figure 3C). They have gone through amphibolite-facies metamorphism and are mainly composed of plagioclase, amphibole, and clinopyroxene, with magnetite as the accessory mineral (Figure 3D). Anhedral or sub-euhedral clinopyroxene and amphibole crystals are in between lath-shaped plagioclase crystals and the crystallization sequence is plagioclase-clinopyroxene. The isotropic gabbros transition gradually into massive basalts, which have a pillow structure on top of the lava flow. Basalt pillows range from 20 to 50 cm in diameter and quenched margins can be seen in the field (Figure 3E). They consist of olivine phenocrysts within a fine-grained groundmass of plagioclase, clinopyroxene and glasses (Figure 3F). Basaltic dykes or veins can be seen intruding into cumulate gabbros in the field (Figure 3G,H), which indicates the cumulate gabbros formed earlier than the pillow basalts and the isotropic gabbros. The peridotites, which are highly serpentinized, are mainly bordered by cumulate gabbros along faults.

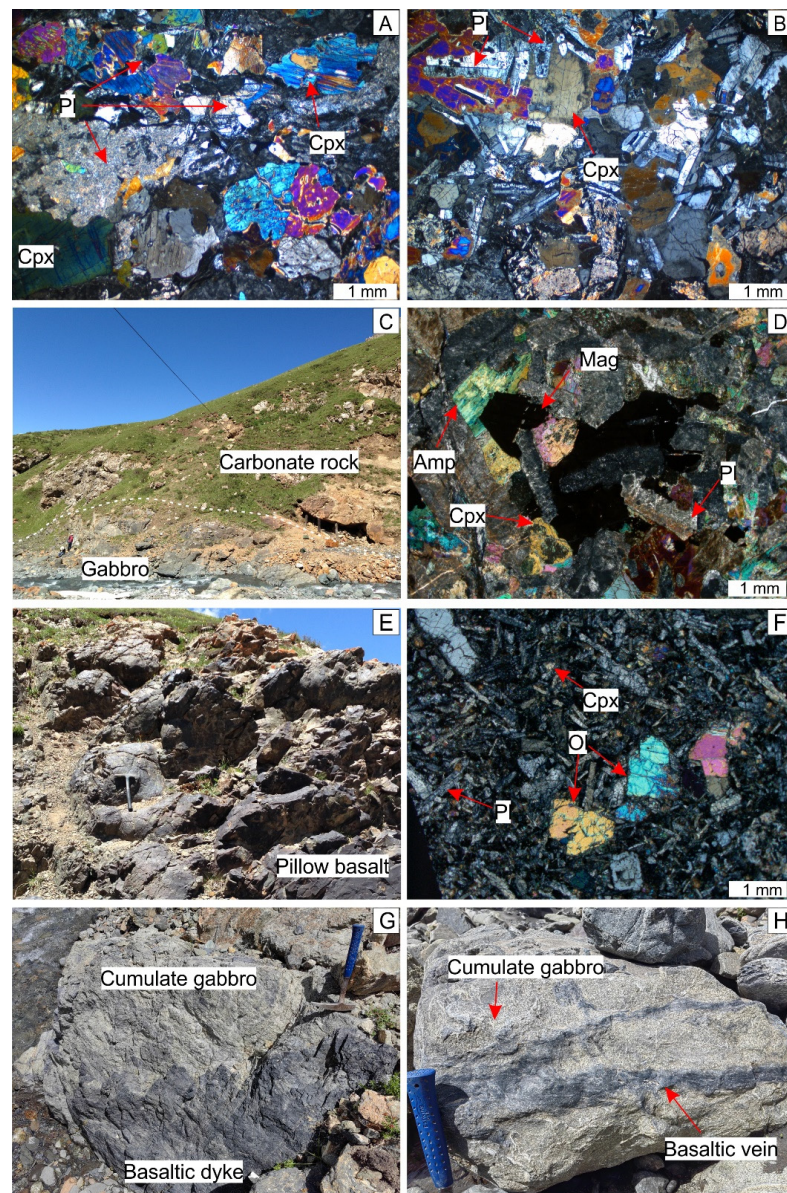


**Figure 3.** Field photos and photomicrographs of mafic rocks in the study area. (A) Cumulate texture of 13HC-025 under cross-polarized light (XPL) view with plagioclase as the cumulate mineral and

anhedral clinopyroxene as the intercumulus mineral. (B) The ophitic texture of diabase 13HC-015 under XPL view. (C) The isotropic gabbro 14HC-005-1 intrudes into carbonate rock. (D) The isotropic gabbro 14HC-005-1 under XPL view with plagioclase and clinopyroxene as the main mineral phase. Several clinopyroxene crystals are replaced by amphibole. (E) The pillow basalt 14HC-003 with pillows ranging from 20 to 50 cm in diameter. (F) The pillow basalt 14HC-003 under XPL view with olivine as phenocryst and plagioclase and glass in the groundmass. (G) Basaltic magma intruded into cumulate gabbros showing as dykes. (H) Basaltic magma intruded into cumulate gabbro showing as veins.

#### 4.2. Whole Rock Geochemistry

The pillow basalts and the isotropic gabbro are plotted along the boundary of the alkaline and subalkaline series in the total alkali silica (TAS) diagram (Figure 4A) and in the field of alkaline basalt in Figure 4B, indicating they are alkaline rocks. The content of  $\text{Al}_2\text{O}_3$  in cumulate gabbros and diabases are higher than that of the isotropic gabbro and pillow basalts (Figure 4C). Furthermore, the  $\text{Eu}_N/\text{Eu}^*$  ( $2\text{Eu}_N/(\text{Sm}_N+\text{Gd}_N)$ ; chondrite normalised) for the cumulate gabbros (1.58–2.50) and diabases (1.27–1.34) are also higher than those in the isotropic gabbro (1.20) and pillow basalts (0.86–1.07) (Figure 4E). This evidence suggests cumulate gabbros and diabases in this study have undergone through plagioclase accumulation. The  $\text{CaO}/\text{Al}_2\text{O}_3$  in the cumulate gabbros and diabases are higher than those in the pillow basalts and the isotropic gabbro and it increases with decreasing  $\text{SiO}_2$  indicating clinopyroxene accumulation (Figure 4D). The pillow basalts are overall richer in incompatible elements than those in the cumulate gabbros and diabases (Figure 4F–H). All these integrations indicate that the cumulate gabbros and diabases are crystal assemblages with or without fractionated melts. The REE of the cumulate gabbros range from LREE-depleted to LREE-enriched ( $\text{La}/\text{Yb} = 0.67\text{--}1.55$ ), while the REE of the diabases are flat ( $\text{La}/\text{Yb} = 1.01\text{--}1.12$ ). The pillow basalts and the isotropic gabbro are rich in LREE with  $\text{La}/\text{Yb}$  of 1.28–1.7. On the N-MORB normalised multi-element diagram, Th and La in the pillow basalts and the isotropic gabbro show slight enrichment relative to Nb (Figure 4G).

#### 4.3. SHRIMP Zircon Geochronology

Zircon crystals sampled from a cumulate gabbro and a diabase display oscillatory zoning or wide band, with a grain length of 50–100  $\mu\text{m}$  and aspect ratios of 1:1–3:1 (Figure 5). Zircons in the isotropic gabbro are 100–250  $\mu\text{m}$  in length with aspect ratios of 1:1 to 4:1. These crystals have wide bands and do not display oscillatory zoning.

Fourteen analyses were achieved for the cumulate gabbro (sample 13HC-025-1). Thirteen were plotted on or near concordia (Figure 6A), ranging from 1827 Ma to 121 Ma. Three old dates ( $^{207}\text{Pb}/^{206}\text{Pb}$  age of  $1827 \pm 18$  Ma,  $1001 \pm 17$  Ma and  $975 \pm 26$  Ma;  $\text{Th} = 85\text{--}201$  ppm,  $\text{U} = 308\text{--}714$  ppm,  $\text{Th}/\text{U} = 0.11\text{--}0.65$ ) are from oscillatory zircons with the dates of  $1001 \pm 17$  Ma and  $975 \pm 26$  Ma yielding a weighted average age of  $993 \pm 28$  Ma (MSWD = 0.7). The rest range from 884 Ma to 116 Ma ( $\text{Th} = 88\text{--}2461$  ppm,  $\text{U} = 102\text{--}2082$  ppm,  $\text{Th}/\text{U} = 0.19\text{--}1.48$ ) with two weighted average dates of  $236 \pm 7$  Ma (MSWD = 0.0032,  $n = 2$ ) and  $130 \pm 11$  Ma (MSWD = 3.5,  $n = 3$ ) (Figure 6A).

Twenty-two analyses were achieved for the diabase (sample 13HC-015-1). Thirteen are plotted on or near to concordia ranging from 1761 to 162 Ma ( $\text{Th} = 36\text{--}1959$  ppm,  $\text{U} = 254\text{--}2510$  ppm,  $\text{Th}/\text{U} = 0.11\text{--}1.47$ ) (Figure 6B). Two weighted average dates are obtained:  $1442 \pm 84$  Ma (MSWD = 2.2,  $n = 3$ ;  $\text{Th}/\text{U} = 0.37\text{--}0.75$ ) and  $1093 \pm 21$  Ma (MSWD = 1.18,  $n = 3$ ;  $\text{Th}/\text{U} = 0.11\text{--}0.34$ ). Two dates of  $489 \pm 10$  Ma (spot 6.1;  $\text{Th}/\text{U} = 1.25$ ) and  $297 \pm 6$  Ma (spot 3.1;  $\text{Th}/\text{U} = 0.61$ ) are from two oscillatory zircon crystals (Figure 5).

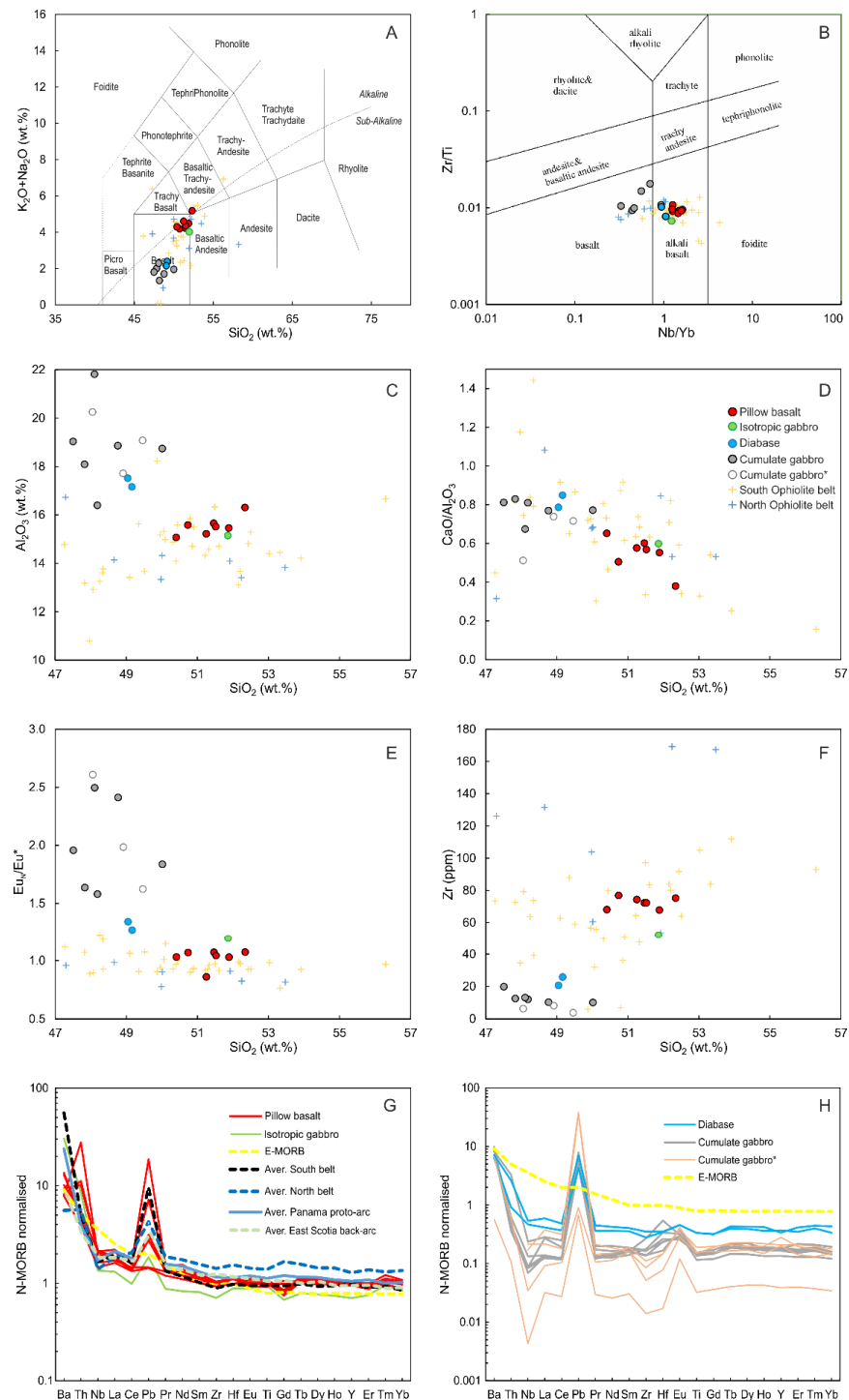


**Figure 4.** The plot of major and trace elements. (A) TAS diagram. (B) Nb/Yb vs. Zr/Ti discrimination diagram. (C) Plagioclase crystallization in SiO<sub>2</sub> vs. Al<sub>2</sub>O<sub>3</sub>. (D) Clinopyroxene crystallization in SiO<sub>2</sub> vs. CaO/Al<sub>2</sub>O<sub>3</sub>. (E) Plagioclase crystallization in SiO<sub>2</sub> vs. Eu<sub>N</sub>/Eu\*. Eu<sub>N</sub> is chondrite normalized and Eu\* = 2Eu<sub>N</sub>/(Sm<sub>N</sub>+Gd<sub>N</sub>). (F) SiO<sub>2</sub> vs. Zr. Cumulate gabbros have lower content of the incompatible trace element Zr than pillow basalts and isotropic gabbros. (G) N-MORB normalized multi-element diagram for pillow basalts and isotropic gabbros. (H) N-MORB normalized multi-element diagram for cumulate gabbros. Mafic rocks in South Ophiolite Belt are from [31,33,36–38,54]. Mafic rocks in North Ophiolite Belts are from [45]. Cumulate gabbro\* in Yushigou and Dongcaohe are from [33] and [38] respectively. Panama proto-arc rocks are from [15]. E-MORB is from [55]. East Scotia back-arc basalts are from GEOROC database (accessed in October 2019).



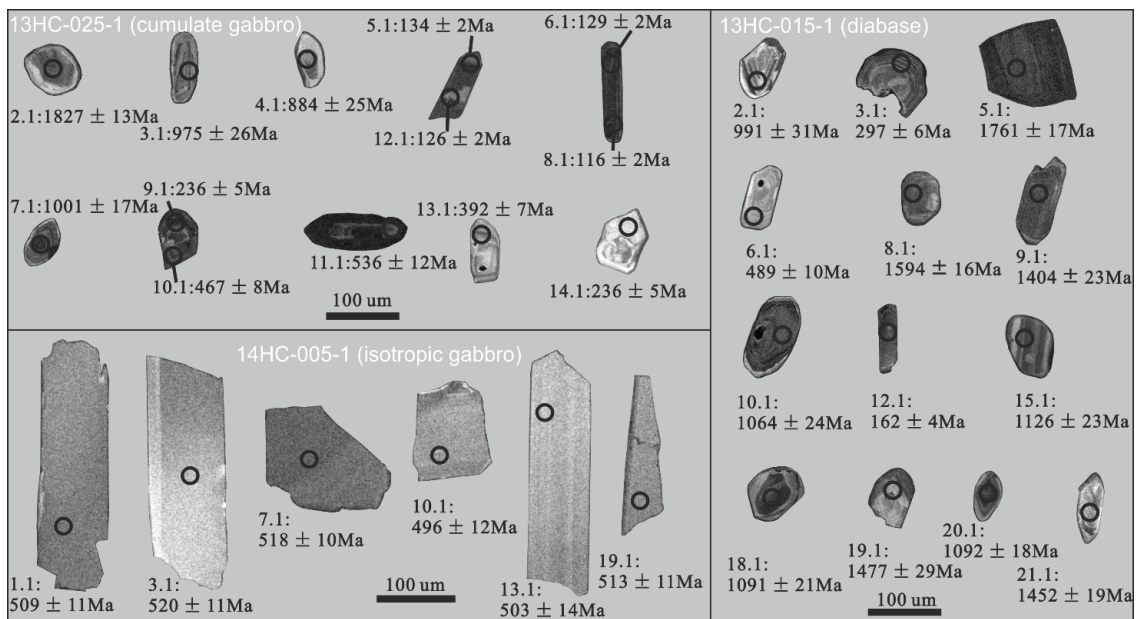


Figure 5. CL images for representative zircon crystals (black circles represent analyzing spots).

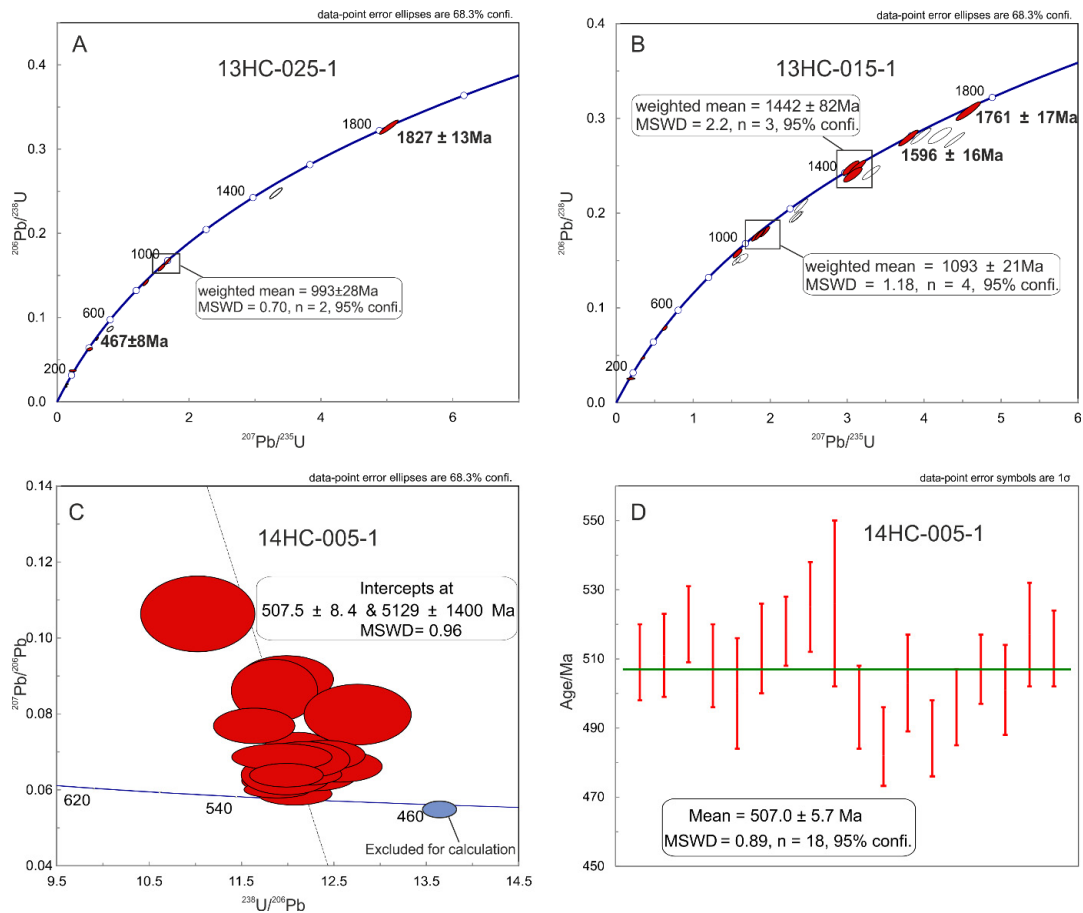


Figure 6. SHRIMP zircon U-Pb concordia plots of (A) Concordia plots for sample 13HC-025-1, (B) Concordia plots for sample 13HC-015-1, (C) Concordia plots for sample 14HC-005-1, and (D) Calculation for the weighted mean age for sample 14HC-005-1. Filled eclipses are analyses on concordia and eclipses are analyses not on concordia. Blue solid lines in (A–C) are concordant line and the black dashed line in (C) is discordant line.



Zircon analyses are relatively homogeneous for the isotropic gabbro (sample 14HC-005-1), with  $^{206}\text{Pb}/^{238}\text{U}$  ages mainly ranging from 482 to 526 Ma (Th = 7–175 ppm, U = 19–229 ppm, Th/U = 0.37–0.85) with one small value of 417 Ma (Th = 195 ppm, U = 199 ppm, Th/U = 0.98). All analyses are within uncertainty of one another and are on or near to concordia (Figure 6C). Eighteen from nineteen analyses yield a weighted average date of  $507 \pm 6$  (MSWD = 0.89; Figure 6D), which is consistent with the lower intercept date on the  $^{238}\text{U}/^{206}\text{Pb}$  versus  $^{207}\text{Pb}/^{206}\text{Pb}$  diagram (Figure 6C).

## 5. Discussion

### 5.1. Hydrous Magmas in a Suprasubduction Zone

Crustal contamination seems inevitable when primitive magmas pass through the lithosphere or dwell in magma chambers after melt extraction from mantle sources [56,57]. In Figure 7, no correlation between fractionation indicates  $\text{SiO}_2$  and Th/La or Th/Nb demonstrates that crustal contamination plays a neglectable role in affecting these trace element ratios. The pillow basalts and the isotropic gabbro all plot in the arc field suggesting these rocks could form in a suprasubduction zone, which is consistent with the slight enrichment of Th and La compared with Nb on the N-MORB normalized diagram (Figure 4G). Ratios of Th/La and Th/Nb reflect sediment component [58,59] and higher Th/La and Th/Nb values in pillow basalts and the isotropic gabbro than MORB (Figure 8B) indicates the presence of a sediment component in these rocks. This sediment component is most likely from subducting slab during the process of subduction.

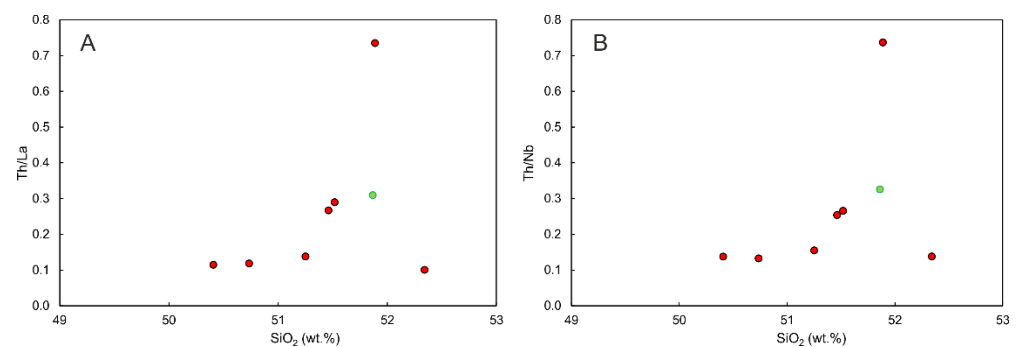


**Figure 7.** Trace element ratios versus  $\text{SiO}_2$  for pillow basalts and the isotropic gabbro. (A)  $\text{SiO}_2$  vs. Th/La and (B)  $\text{SiO}_2$  vs. Th/Nb.

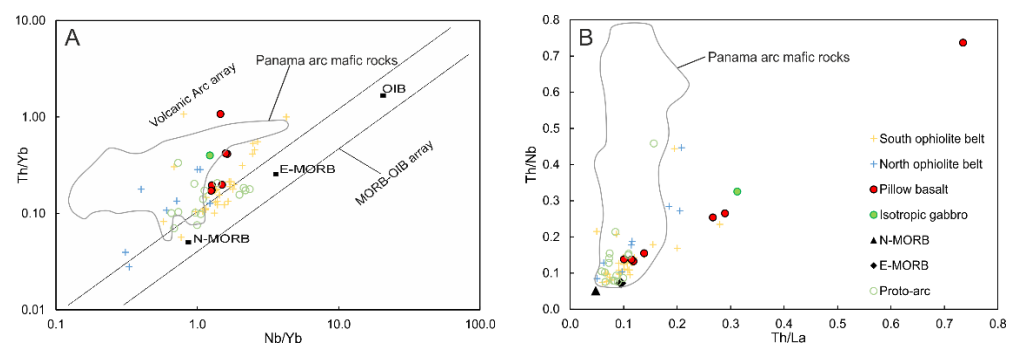


**Figure 8.** Tectonic discrimination for pillow basalts and the isotropic gabbro of (A) Nb/Yb vs. Th/Yb and (B) Th/La vs. Th/Yb. References for data are the same as Figure 4. The Panama arc mafic rocks are Chagres-Bayano arc from [60] and only MgO > 4 wt.% are used.

The cumulate gabbros undergo through plagioclase-clinopyroxene accumulation (Figure 3B) with plagioclase crystallizing before clinopyroxene. High  $\text{Al}_2\text{O}_3$  and positive Eu anomaly also indicate plagioclase accumulation. The low content of incompatible elements demonstrates that the cumulate gabbros are a mineral assemblage without or with

minor evolving melts. Geochemical modelling was conducted using rhyolite-MELTS [61] to test if the cumulate gabbros and the pillow basalts are genetically related and furthermore what the crystallizing condition is. The crystallization sequence in the cumulate gabbro is similar to the one in the MOR setting which occurs under low-pressure conditions [62]. Therefore, low pressures of 1 kbar and 3 kbar with 0%, 1%, and 2% water content were conducted with the pillow basalt 14HC-003-3 as the initial composition. The model of 3 kbar-0% water yielded a result that suggested olivine formed after clinopyroxene was excluded as olivine should crystallize before clinopyroxene. The results of five models (1 kbar-0% water, 1 kbar-1% water, 1 kbar-2% water, 3 kbar-1% water, 3 kbar-2% water) with absent oxygen fugacity were plotted. In Figure 9, the instantaneous accumulated crystal assemblage in both the 1kbar-1% water model and 3 kbar-1% water fits the analyzed data and the 1 kbar-1% water model works better. The model under dry conditions cannot produce cumulate gabbros. The cumulate gabbros and the diabases can be achieved by 10%–25% crystallization in  $\text{SiO}_2$  versus  $\text{Al}_2\text{O}_3$  diagram (Figure 9A) and  $\text{SiO}_2$  versus  $\text{FeO}_t$  diagram (Figure 9C). It is 25%–30% in the  $\text{SiO}_2$  versus  $\text{CaO}$  diagram (Figure 9B) and 10%–30% in the  $\text{SiO}_2$  versus  $\text{MgO}$  diagram (Figure 9D). We then apply the mineral assemblage of this model to trace element modelling. The instantaneous composition of accumulated crystals at  $F = 10\%$ – $30\%$  is highly consistent with the composition of cumulate gabbros. This indicates the cumulate gabbros can be derived from the crystal accumulation of a melt similar to 14HC-003-3 under hydrous conditions. The diabases have a high content of incompatible elements which cannot be achieved by any degrees of crystallization in this model. This might suggest that these diabases are composed not only of accumulated crystals but also fractionated melts.

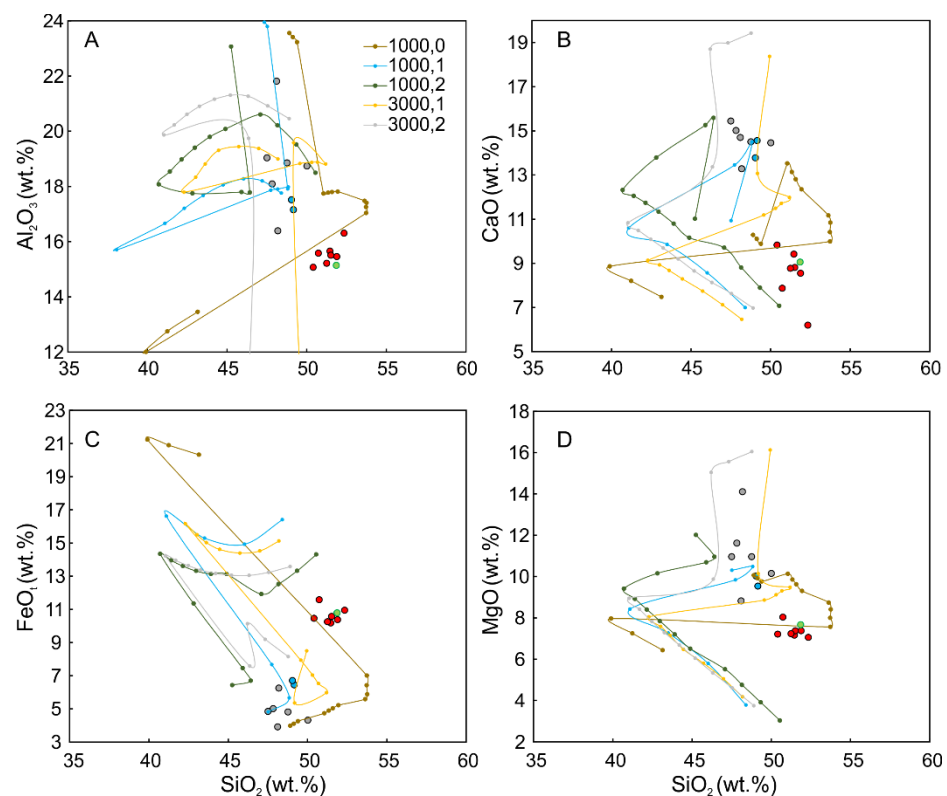


**Figure 9.** Accumulation modelling by rhyolite-MELTS of (A)  $\text{SiO}_2$  vs.  $\text{Al}_2\text{O}_3$ , (B)  $\text{SiO}_2$  vs.  $\text{CaO}$ , (C)  $\text{SiO}_2$  vs.  $\text{FeO}_t$ , and (D)  $\text{SiO}_2$  vs.  $\text{MgO}$ . The initial melt composition is 14HC-3-3 and fractional crystallization is adopted. The accumulation trend for each of the five models (1 kbar-0% water, 1 kbar-1% water, 1 kbar-2% water, 3 kbar-1% water, 3 kbar-2% water) represents the instantaneous crystal assemblage with 5% intervals and it starts from 5% to 70% crystallization.

### 5.2. Origin of Pre-Cambrian Zircon Crystals

The date of 507 Ma for the isotropic gabbro is consistent with the dates derived from mafic rocks in the South Ophiolite Belt (550–515 Ma for Yushigou and 500–497 Ma for the rest; [16,18,31,33,36–38]). This date is interpreted as the crystallization age of the isotropic gabbro. No zircon crystals of a similar age were found in the cumulate gabbros and diabases suggesting that the zircon was undersaturated during magmatic cooling. The field observation basaltic magma intruding into cumulate gabbros (Figure 3G,H) demonstrates the cumulate gabbros formed earlier than the basalts, i.e., the cumulate gabbros are older than ca. 507 Ma. The pre-Cambrian zircon crystals in the cumulate gabbro and the diabase can be divided into three groups: 1700–1800 Ma, ~1440 Ma, and 1000–1100 Ma. As can be seen from the compiled zircon dates from Proterozoic metamorphic rocks (Figure 10), ~1440 Ma, and 1000–1100 Ma in the present study can be seen in the pre-Cambrian basement of the NQOB while all these three age groups can be found in the Qilian Block. Furthermore, a 476 Ma Minleyaogou granodiorite possesses old inherited zircons of 1395 Ma, 1042 Ma, and 976 Ma [63] which are consistent with the dates of zircon xenocrysts in the present study. Therefore, the zircons might be captured from the pre-Cambrian continental crust (e.g., in continental rift or continental convergent margin) during magma ascent. The young date of ~417 Ma from 14HC-005 could be a metamorphic age corresponding to the exhumation of subducted continent [16] while the date of ~130 Ma and ~236 Ma from 13HC-025-1 could be a metamorphic age related to the ~167 Ma magmatism event [64] and the ~228 Ma metamorphism event [65] respectively. This is also supported by zircon morphology as the young zircons such as 5.1 and 6.1 in sample 13HC-025-1 and 12.1 in 13HC-015-1 (Figure 5) are lath-shaped similar to zircon crystals formed in fluids [66].

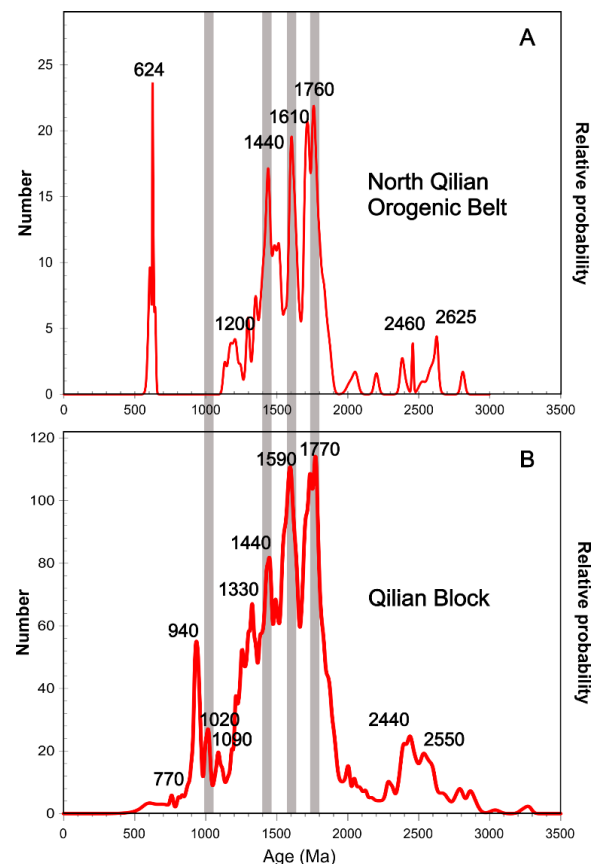


**Figure 10.** Precambrian detrital zircons in the Proterozoic metamorphic rocks. (A) Distribution for detrital zircons from the NQOB. The data (Beidahe group and Tuolai group) are from [30,67,68]. (B) Distribution of detrital zircons from the Qilian Block. The data (Gaolan group and Huangyuan group, and Tuolai group) are from [28–30].

The alkaline granite (with aegirine augite as the accessory mineral) of 501 Ma intruding into serpentinite in Chuancigou (~8 km southeast; [46]) shows enrichment of Ba, Th, and light rare earth elements on the N-MORB normalized multi-element diagram (Figure 11B). This trace element characteristic cannot be achieved by fractional crystallization of the basaltic magma of 14HC-003-3 (Figure 11B). However, they are similar to continent crust suggesting this alkaline granite, synchronous to the formation of the isotropic gabbro, should have components of the continent crust. This supports the interpretation that the mafic rocks in Hongtugou and the nearby areas at ca. 500 Ma formed in a continent-related tectonic setting.

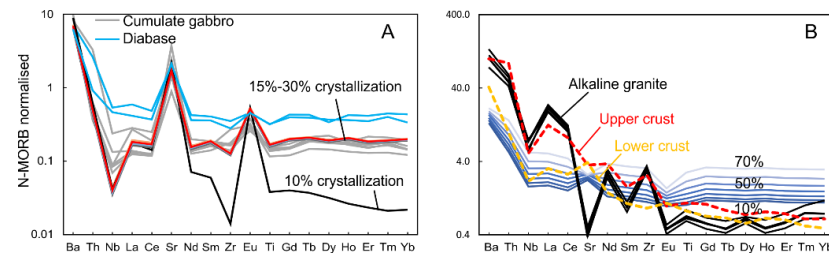


**Figure 11.** Trace element modelling for fractional crystallization. The initial composition is 13HC-003-3 and the mineral phases are from MELTS modelling. **(A)** Mineral accumulation process. The cumulate is instantaneous mineral assemblage so the equation for fractional crystallization, i.e.,  $C_{\text{Residual}} = C_0 \times D \times F^{(D-1)}$  is adopted. **(B)** Melt composition due to fractionation process. The blue lines are the melt composition with 10% interval ranging from 10% to 70% crystallization. The equation  $C_{\text{Melt}} = C_0 \times F^{(D-1)}$  is adopted. The alkaline granite is from Wang et al. (2018) [46].

### 5.3. Tectonic Setting and Implications

The Hongtugou mafic rocks show slab components (Th-La enrichment relative to Nb and high Th/La and Th/Nb) and are believed to have formed in a hydrous environment, consistent with a SSZ setting. The presence of the pre-Cambrian zircon xenocrysts indicates that the Hongtugou mafic rocks formed in the continental convergent margin such as continental arc/forearc. A continental back-arc is an unlikely setting, as magmas generated here are not significantly affected by slab components as the spreading ridge is far away from the trench (e.g., the subduction in Japan and Rocas Verdes back-arc ophiolite in Chile [69,70]), as can be seen from the East Scotia Ridge basalts (Figure 4G). In addition, the FAB-like tholeiite and boninite in Dachadaban (Figure 1) in the north of Hongtugou indicate subduction initiation (northward subduction) at ca. 517 Ma [41], which also argues against a continental back-arc spreading in Hongtugou and the South Ophiolite Belt at this time. The rock assemblage of peridotite (serpentinized)  $\pm$  cumulate ultramafic rock + cumulate gabbro + isotropic gabbro + pillow basalt forms the complete sequence of ophiolite whereby this rock assemblage in the South Ophiolite Belt is considered as ophiolite. They are considered to form in the middle ocean ridge as the mafic rocks such as basalts and isotropic gabbros show similarity to MORB [16,31,33,38]. Ophiolites mark the growth of the oceanic lithosphere and the continent-related ophiolite includes continental margin ophiolite which forms during continental rifting and continental back-arc ophiolite which forms during back-arc rifting [4]. Therefore, the present study suggests the rock assemblage in Hongtugou does not fall into any ophiolite category of Dilek and Furnes (2011) [4]. The mafic rocks and serpentinized peridotite in the South Ophiolite Belt are often bounded by faults [33,38] and the peridotite might be better classified as orogenic peridotite [17].

Determining the tectonic settings of igneous rocks can be sometimes challenging. For example, the tectonic setting for the Oman ophiolite is highly debated as to whether it is formed in MOR or SSZ [71,72]. The wet condition of crystallization argues for a SSZ affinity and the mafic rocks probably formed shortly after subduction initiation [72]. The pillow basalts and isotropic gabbro in the present study are similar to the proto-arc rocks in the



fore-arc area in central America according to slight Th and La enrichment relative to Nb on the N-MORB normalized multi-element diagram (Figure 4G). Furthermore, both the pillow basalt and the Panamanian proto-arc rocks plot in the arc field show higher Th/Nb and Th/La than MORB (Figure 8). This might suggest the pillow basalts and the isotropic gabbro in the present study formed shortly after subduction initiation with the mantle source being metasomatized by only a minor slab component, similar to the proto-arc in Panama [15].

The subduction direction is also controversial in the NQOB as some suggest northward subduction [16,41] and others suggest southward subduction [18,39]. Qilian ocean spreading continued from ca. 710 Ma till 520 Ma when subduction initiated (Figure 12A) [16]. The southward subduction initiation occurred prior to ca. 512 Ma, as represented by the Kekeli pluton in the north margin of Qilian Block [39], ca. 20 km south of Hongtugou (Figure 1). More plutons of a similar age were discovered in the eastern part [36,40]. The northward subduction is mainly based on the observation that the back-arc (the North Ophiolite Belt) sits behind the continental arc belt to the north [16]. Subduction initiated in this continental arc at ca. 517 Ma as represented by the MORB-like tholeiitic magmatism in Dachadaban [41], followed by boninite and continental arc magmatism from 516 to 494 Ma [16,41,43] while the back-arc spreading occurred from 490 Ma to 448 Ma [16]. The present study cannot determine the subduction polarity. However, the crystallization age of the isotropic gabbro is consistent with both the intermediate-felsic plutons in the north margin of the Qilian Block (Figure 12B) and the arc magmatism in the continental arc belt (Figure 12C), which supports the idea that the mafic rocks in Hongtugou formed in a continental convergent margin. The present work along with the previous study on the alkaline granite in the nearby Chuancigou [46] further suggests it might be an extensional convergent margin formed shortly after subduction initiation, e.g., a continental fore-arc or arc. The model in the present study can better explain why the mafic rocks preserved in the South Ophiolite Belt show similar crystallization age. Subduction initiation is a rapid process which takes <10 Ma to transit from FAB to normal arc magmatism [14]. Besides, it propagates rapidly away from the site of subduction initiation nucleation [73,74]. These two characteristics restrict the crystallization ages of mafic rocks in the present study in a narrow range, while the previous MOR-ophiolite model is difficult to address this question and also the question of preservation of subducted oceanic lithosphere. Detailed future studies should focus on determining the relationship between the mafic rocks and the peridotite and extending the research to the nearby area.

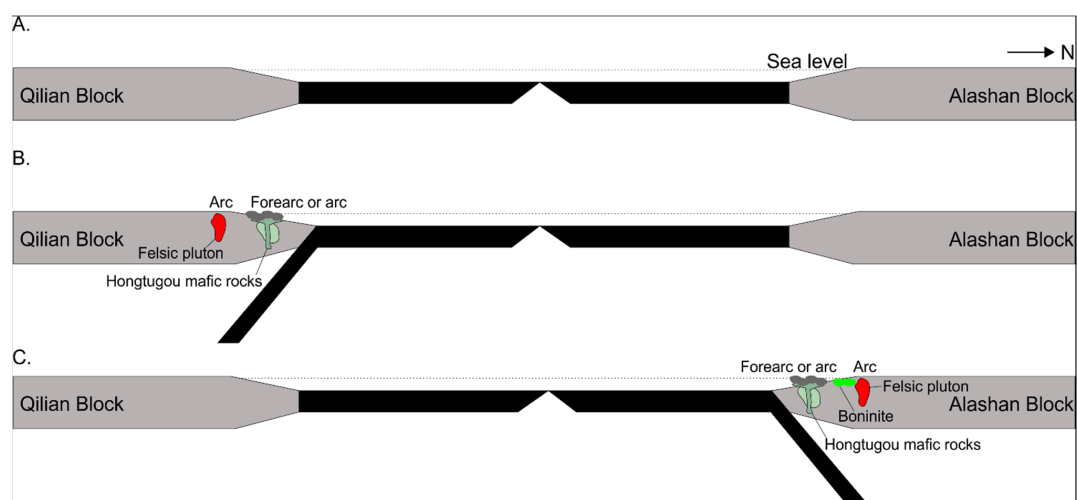


**Figure 12.** Tectonic evolution of the NQOB to illustrate a continental convergent margin setting for mafic rocks in the present study. (A) Stage I: Qilian Ocean spreading (ca 710–520 Ma), (B) Stage II-Hypothesis one: Southward subduction (ca. 507 Ma), and (C) Stage II-Hypothesis two: Northward subduction (ca. 507 Ma). The ages for Qilian Ocean spreading are from Song et al. (2013) [16].

## 6. Conclusions

The Hongtugou mafic rocks consist of cumulate gabbros, diabases, isotropic gabbros, and basalts. Zircon SHRIMP U-Pb dating yields a concordia age of  $507 \pm 6$  Ma for the isotropic gabbro which is consistent with the crystallization ages of other mafic rocks in the South Ophiolite Belt of the NQOB. Slight enrichment of Th and La relative to Nb on the N-MORB normalized multi-element diagram for the isotropic gabbro and pillow basalts indicates a suprasubduction zone setting. This is supported by the geochemical modelling which suggests a hydrous crystallizing condition for the cumulate gabbros and basalts. Proterozoic zircon xenocrysts in the cumulate gabbros and diabases suggest this suprasubduction zone might be a continental convergent margin such as continental fore-arc or arc. These mafic rocks might form shortly after subduction initiation. The present study provides a new perspective on the mafic-ultramafic rock sequences in the South Ophiolite Belt which are commonly interpreted as MORB-type or SSZ-type ophiolites.

**Supplementary Materials:** The following supporting information can be downloaded at: <https://www.mdpi.com/article/10.3390/min12091105/s1>, Table S1: Whole rock geochemical data; Table S2: SHRIMP zircon data.

**Author Contributions:** Conceptualization, G.S. and J.W.; methodology, G.S. and G.X.; validation, J.W.; formal analysis, J.W.; investigation, G.X., J.W., J.N. and G.S.; data curation, G.X. and J.W.; writing—original draft preparation, J.W.; writing—review and editing, G.S.; visualization, J.W.; supervision, G.S.; project administration, G.S. and G.X.; funding acquisition, G.S. and G.X. All authors have read and agreed to the published version of the manuscript.

**Funding:** This research was funded by Second Tibetan Plateau Scientific Expedition and Research Program (STHP), grant no. 2019QZKK0802.

**Institutional Review Board Statement:** Not applicable.

**Informed Consent Statement:** Not applicable.

**Data Availability Statement:** Data is available within the Supplementary Materials.

**Acknowledgments:** We thank local Tibetan residents who provide us accommodation during the field work which is precious in the remote Qilian area. We thank Lilong Yan for scientific discussions which are helpful for this manuscript. We thank William D. Smith for improving this paper's language. We thank two reviewers for their in-depth advice which improve the manuscript a lot.

**Conflicts of Interest:** The authors declare no conflict of interest.

## References

1. Kusky, T.M.; Windley, B.F.; Safonova, I.; Wakita, K.; Wakabayashi, J.; Polat, A.; Santosh, M. Recognition of ocean plate stratigraphy in accretionary orogens through Earth history: A record of 3.8 billion years of sea floor spreading, subduction, and accretion. *Gondwana Res.* **2013**, *24*, 501–547. [[CrossRef](#)]
2. Xiao, W.; Windley, B.F.; Indiana, H. Late Paleozoic to early triassic multiple roll-back and oroclinal bending of the Mongolia collage in central Asia. *Earth-Sci. Rev.* **2018**, *186*, 94–128. [[CrossRef](#)]
3. Miyashiro, A. The Troodos ophiolitic complex was probably formed in an island arc. *Earth Planet. Sci. Lett.* **1973**, *19*, 218–224. [[CrossRef](#)]
4. Dilek, Y.; Furnes, H. Ophiolite genesis and global tectonics: Geochemical and tectonic fingerprinting of ancient oceanic lithosphere. *Bull. Geol. Soc. Am.* **2011**, *123*, 387–411. [[CrossRef](#)]
5. Pearce, J.A. Immobile element fingerprinting of ophiolites. *Elements* **2014**, *10*, 101–108. [[CrossRef](#)]
6. Dilek, Y.; Furnes, H. Ophiolites and their origins. *Elements* **2014**, *10*, 93–100. [[CrossRef](#)]
7. Bodinier, J.L.; Godard, M. *Orogenic, Ophiolitic, and Abyssal Peridotites*, 3rd ed.; Elsevier: Amsterdam, The Netherlands, 2013; Volume 3, ISBN 9780080983004.
8. Menzies, M.A.; Dupuy, C. Orogenic Massifs: Protolith, Process and Provenance. *J. Petrol.* **1991**, *2*, 1–16. [[CrossRef](#)]
9. Downes, H.; Bodinier, J.-L.; Thirlwall, M.F.; Lorand, J.-P.; Fabries, J. REE and Sr-Nd Isotopic Geochemistry of Eastern Pyrenean Peridotite Massifs: Sub-Continental Lithospheric Mantle Modified by Continental Magmatism. *J. Petrol.* **1991**, *29*, 97–115. [[CrossRef](#)]
10. Pearce, J.A.; Peate, D.W. Tectonic implications of the composition of volcanic arc magmas. *Annu. Rev. Earth Planet. Sci.* **1995**, *23*, 251–285. [[CrossRef](#)]

11. Tatsumi, Y. The subduction factory: How it operates in the evolving Earth. *GSA Today* **2005**, *15*, 4. [[CrossRef](#)]
12. Reagan, M.K.; Ishizuka, O.; Stern, R.J.; Kelley, K.A.; Ohara, Y.; Blichert-Toft, J.; Bloomer, S.H.; Cash, J.; Fryer, P.; Hanan, B.B.; et al. Fore-arc basalts and subduction initiation in the Izu-Bonin-Mariana system. *Geochem. Geophys. Geosyst.* **2010**, *11*, Q03X12. [[CrossRef](#)]
13. Reagan, M.K.; Pearce, J.A.; Petronotis, K.; Almeev, R.R.; Avery, A.J.; Carvallo, C.; Chapman, T.; Christeson, G.L.; Ferré, E.C.; Godard, M.; et al. Subduction initiation and ophiolite crust: New insights from IODP drilling. *Int. Geol. Rev.* **2017**, *59*, 1439–1450. [[CrossRef](#)]
14. Ishizuka, O.; Tani, K.; Reagan, M.K.; Kanayama, K.; Umino, S.; Harigane, Y.; Sakamoto, I.; Miyajima, Y.; Yuasa, M.; Dunkley, D.J. The timescales of subduction initiation and subsequent evolution of an oceanic island arc. *Earth Planet. Sci. Lett.* **2011**, *306*, 229–240. [[CrossRef](#)]
15. Buchs, D.M.; Arculus, R.J.; Baumgartner, P.O.; Baumgartner-Mora, C.; Ulianov, A. Late Cretaceous arc development on the SW margin of the Caribbean Plate: Insights from the Golfito, Costa Rica, and Azuero, Panama, complexes. *Geochem. Geophys. Geosyst.* **2010**, *11*, Q07S24. [[CrossRef](#)]
16. Song, S.; Niu, Y.; Su, L.; Xia, X. Tectonics of the North Qilian orogen, NW China. *Gondwana Res.* **2013**, *23*, 1378–1401. [[CrossRef](#)]
17. Song, S.; Su, L.; Niu, Y.; Lai, Y.; Zhang, L. CH<sub>4</sub> inclusions in orogenic harzburgite: Evidence for reduced slab fluids and implication for redox melting in mantle wedge. *Geochim. Cosmochim. Acta* **2009**, *73*, 1737–1754. [[CrossRef](#)]
18. Zuzva, A.V.; Wu, C.; Reith, R.C.; Yin, A.; Li, J.; Zhang, J.; Zhang, Y.; Wu, L.; Liu, W. Tectonic evolution of the Qilian Shan: An early Paleozoic orogen reactivated in the Cenozoic. *GSA Bull.* **2018**, *130*, 881–925. [[CrossRef](#)]
19. Xu, Z.; Yang, J.; Zhang, J.; Jiang, M.; Li, H.; Cui, J. A comparison between the tectonic units on the two sides of the Altun sinistral strike-slip fault and the mechanism of lithospheric shearing. *Acta Geol. Sin.* **1999**, *73*, 193–205.
20. Li, X.; Su, L.; Song, B.; Liu, D. SHRIMP U-Pb zircon age of the Jinchuan ultramafic intrusion and its geological significance. *Chin. Sci. Bull.* **2004**, *49*, 420. [[CrossRef](#)]
21. Xiu, Q.; Yu, H.; Li, Q.; Zuo, G.; Cao, C. Discussion on the Petrogenic Time of Longshoushan Group, Gansu Province. *Acta Geol. Sin.* **2004**, *78*, 366–373.
22. Geng, Y.S.; Wang, X.S.; Shen, Q.H.; Wu, C.M. Redefinition of the Alxa Group-complex (Precambrian metamorphic basement) in the Alxa area, Inner Mongolia. *Geol. China* **2006**, *33*, 138–145.
23. Geng, Y.S.; Wang, X.S.; Shen, Q.H.; Wu, C.M. Chronology of the Precambrian metamorphic series in the Alxa area, Inner Mongolia. *Geol. China* **2007**, *34*, 251–261.
24. Tung, K.; Yang, H.-J.; Yang, H.-Y.; Liu, D.; Zhang, J.; Wan, Y.; Tseng, C.-Y. SHRIMP U-Pb geochronology of the zircons from the Precambrian basement of the Qilian Block and its geological significances. *Chin. Sci. Bull.* **2007**, *52*, 2687–2701. [[CrossRef](#)]
25. Li, X.H.; Su, L.; Chung, S.; Li, Z.-X.; Liu, Y.; Song, B.; Liu, D.Y. Formation of the Jinchuan ultramafic intrusion and the world's third largest Ni-Cu sulfide deposit: Associated with the ~825 Ma south China mantle plume? *Geochem. Geophys. Geosyst.* **2005**, *6*, Q11004. [[CrossRef](#)]
26. Li, Y.; Tong, X.; Zhu, Y.; Lin, J.; Zheng, J.; Brouwer, F.M. Tectonic affinity and evolution of the Precambrian Qilian block: Insights from petrology, geochemistry and geochronology of the Hualong Group in the Qilian Orogen, NW China. *Precambrian Res.* **2018**, *315*, 179–200. [[CrossRef](#)]
27. Tung, K.-A.; Yang, H.-Y.; Liu, D.-Y.; Zhang, J.-X.; Yang, H.-J.; Shau, Y.-H.; Tseng, C.-Y. The amphibolite-facies metamorphosed mafic rocks from the Maxianshan area, Qilian block, NW China: A record of early Neoproterozoic arc magmatism. *J. Asian Earth Sci.* **2012**, *46*, 177–189. [[CrossRef](#)]
28. Liu, C.; Wu, C.; Zhou, Z.; Yan, Z.; Jiang, T.; Song, Z.; Liu, W.; Yang, X.; Zhang, H. U-Pb detrital zircon geochronology from the basement of the Central Qilian Terrane: Implications for tectonic evolution of northeastern Tibetan Plateau. *Int. J. Earth Sci.* **2018**, *107*, 673–686. [[CrossRef](#)]
29. Li, Z.; Li, Y.; Xiao, W.; Zheng, J.; Brouwer, F.M. Geochemical and zircon U-Pb-Hf isotopic study of metasedimentary rocks from the Huangyuan Group of the Central Qilian block (NW China): Implications for paleogeographic reconstruction of Rodinia. *Precambrian Res.* **2020**, *351*, 105947. [[CrossRef](#)]
30. Gao, Y.; Long, X.; Luo, J.; Dong, Y.; Lan, C.; Huang, Z.; Zhao, J. Provenance and Hf isotopic variation of Precambrian detrital zircons from the Qilian Orogenic Belt, NW China: Evidence to the transition from breakup of Columbia to the assembly of Rodinia. *Precambrian Res.* **2021**, *357*, 106153. [[CrossRef](#)]
31. Xia, X.H.; Sun, N.; Song, S.G.; Xiao, X.C. Age and tectonic setting of the Aoyougou-Erzhihaladaban ophiolite in the western North Qilian Mountains, NW China. *Acta Sci. Nat. Univ. Pekin.* **2012**, *48*, 757–769.
32. Xiang, Z.Q.; Lu, S.N.; Li, H.K.; Li, H.M.; Song, B.; Zheng, J.K. SHRIMP U-Pb zircon age of gabbro in Aoyougou in the western segment of the North Qilian Mountains, China and its geological implications. *Geol. Bull. China* **2007**, *26*, 1686–1691.
33. Shi, R.; Yang, J.; Wu, C.; Wooden, J. First SHRIMP dating for the formation of the Late Sinian Yushigou ophiolite, North Qilian Mountains. *ACTA Geol. Sin. Ed.* **2004**, *78*, 649–657.
34. Wang, G.; Li, X.; Yu, J.; Tang, Z.; Zhu, T.; Pan, F.; Zhang, Y.; Bu, T. LA-ICP-MS zircon U-Pb dating of syenite from Yushigou in Northern Qilian Mountain. *Geol. Bull. China* **2018**, *37*, 532–537.
35. Li, B.; Hu, D.; Chen, X.; Zhang, Y.; Wu, H.; Wang, C. Zircon U-Pb Age of Granite Porphyry Within Youhulugou Ophiolite in the Suture Zone of North Qilian Mountains and Its Geological Implications. *Geoscience* **2017**, *31*, 1170.

36. Fu, C.; Yan, Z.; Aitchison, J.C.; Xiao, W.; Buckman, S.; Wang, B.; Li, W.; Li, Y.; Ren, H. Multiple subduction processes of the Proto-Tethyan Ocean: Implication from Cambrian intrusions along the North Qilian suture zone. *Gondwana Res.* **2020**, *87*, 207–223. [[CrossRef](#)]
37. Wu, P.; Li, X.; Xu, X.; Yu, J.; Sun, J.; Tang, Z.; Wang, G. LA-ICP-MS zircon U-Pb dating and geochemical characteristics of Donggou ophiolites in Zamashi area of northern Qilian Mountain. *Geol. Bull. China* **2012**, *31*, 896–906.
38. Tseng, C.-Y.; Yang, H.-J.; Yang, H.-Y.; Liu, D.; Tsai, C.-L.; Wu, H.; Zuo, G. The Dongcaohe ophiolite from the North Qilian Mountains: A fossil oceanic crust of the Paleo-Qilian ocean. *Chin. Sci. Bull.* **2007**, *52*, 2390–2401. [[CrossRef](#)]
39. Wu, C.; Xu, X.; Gao, Q.; Li, X.; Lei, M.; Gao, Y.; Frost, R.B.; Wooden, J.L. Early Palaeozoic granitoid magmatism and tectonic evolution in North Qilian, NW China. *Acta Petrol. Sin.* **2010**, *26*, 1027–1044.
40. Peng, Y.B.; Yu, S.Y.; Zhang, J.X.; Li, S.Z.; Sun, D.Y.; Tong, L.X. Early Paleozoic arc magmatism and metamorphism in the northern Qilian Block, western China: A case study of Menyuan-Kekeli. *Acta Petrol. Sin.* **2017**, *33*, 3925–3941.
41. Xia, X.; Song, S.; Niu, Y. Tholeiite–boninite terrane in the North Qilian suture zone: Implications for subduction initiation and back-arc basin development. *Chem. Geol.* **2012**, *328*, 259–277. [[CrossRef](#)]
42. Meng, F.C.; Zhang, J.X.; Guo, C.M.; Li, J.P. Constraints on the evolution of the North Qilian ocean basin: MOR-type and SSZ-type ophiolites from Dachadaban. *Acta Petrol. Mineral.* **2010**, *29*, 453–466.
43. Chen, Y.; Song, S.; Niu, Y.; Wei, C. Melting of continental crust during subduction initiation: A case study from the Chaidanuo peraluminous granite in the North Qilian suture zone. *Geochim. Cosmochim. Acta* **2014**, *132*, 311–336. [[CrossRef](#)]
44. Pan, F.; Dong, Y.; Li, X.; Huang, B.; Zhang, Y.; Wang, G.; Yu, J.; Gao, Y.; Zhao, X. Petrogenesis and tectonic setting of Early Paleozoic granites and high-Mg diorites in the Northern Qilian Orogen, China. *J. Asian Earth Sci.* **2020**, *191*, 104250. [[CrossRef](#)]
45. Xia, X.; Song, S. Forming age and tectono-petrogenesis of the Jiugequan ophiolite in the North Qilian Mountain, NW China. *Chin. Sci. Bull.* **2010**, *55*, 1899–1907. [[CrossRef](#)]
46. Wang, J.; Xie, G.; Shi, G.; Wang, Y. Geochronology of the Chuancigou A-type granite in the North Qilian belt and its significances. *ACTA Petrol. Sin.* **2018**, *34*, 1657–1668.
47. Qian, Q.; Zhang, Q.; Sun, X.M. Tectonic setting and mantle source characteristics of Jiugequan basalts, North Qilian: Constraints from trace elements and Nd-isotopes. *Acta Petrol. Sin.* **2001**, *17*, 385–394.
48. Xu, X.; Song, S.; Su, L.; Li, Z.; Niu, Y.; Allen, M.B. The 600–580Ma continental rift basalts in North Qilian Shan, northwest China: Links between the Qilian-Qaidam block and SE Australia, and the reconstruction of East Gondwana. *Precambrian Res.* **2015**, *257*, 47–64. [[CrossRef](#)]
49. Huang, H.; Niu, Y.; Nowell, G.; Zhao, Z.; Yu, X.; Mo, X. The nature and history of the Qilian Block in the context of the development of the Greater Tibetan Plateau. *Gondwana Res.* **2015**, *28*, 209–224. [[CrossRef](#)]
50. Tseng, C.Y.; Yang, H.J.; Yang, H.Y.; Liu, D.; Wu, C.; Cheng, C.K.; Chen, C.H.; Ker, C.M. Continuity of the North Qilian and North Qinling orogenic belts, Central Orogenic System of China: Evidence from newly discovered Paleozoic adakitic rocks. *Gondwana Res.* **2009**, *16*, 285–293. [[CrossRef](#)]
51. Black, L.P.; Kamo, S.L.; Allen, C.M.; Davis, D.W.; Aleinikoff, J.N.; Valley, J.W.; Mundil, R.; Campbell, I.H.; Korsch, R.J.; Williams, I.S.; et al. Improved  $^{206}\text{Pb}/^{238}\text{U}$  microprobe geochronology by the monitoring of a trace-element-related matrix effect; SHRIMP, ID-TIMS, ELA-ICP-MS and oxygen isotope documentation for a series of zircon standards. *Chem. Geol.* **2004**, *205*, 115–140. [[CrossRef](#)]
52. Williams, I.S. U-Th-Pb geochronology by ion microprobe. *Rev. Econ. Geol.* **1998**, *7*, 1–35.
53. Ludwig, K.R. *Isoplot 4.15: A Geochronological Toolkit for Microsoft Excel*; Berkeley Geochronological Center: Berkeley, CA, USA, 2012.
54. Li, B.; Zhang, Y.; Wang, C.; Hu, D. Geochemical characteristics of the Youhulugou basalts in the suture zone of the North Qilian Mountain. *J. Geomech.* **2016**, *22*, 48–55.
55. Sun, S.-S.; McDonough, W. Chemical and isotopic systematics of oceanic basalts: Implications for mantle composition and processes. *Geol. Soc. Lond. Spec. Publ.* **1989**, *42*, 313–345. [[CrossRef](#)]
56. Depaolo, D.J. Trace element and isotopic effects of combined wallrock assimilation and fractional crystallization. *Earth Planet. Sci. Lett.* **1981**, *53*, 189–202.
57. Bohron, W.A.; Spera, F.J.; Giorso, M.S.; Brown, G.A.; Creamer, J.B.; Mayfield, A. Thermodynamic Model for Energy-Constrained Open-System Evolution of Crustal Magma Bodies Undergoing Simultaneous Recharge, Assimilation and Crystallization: The Magma Chamber Simulator. *J. Petrol.* **2014**, *55*, 1685–1717. [[CrossRef](#)]
58. Elliott, T.; Plank, T.; Zindler, A.; White, W.; Bourdon, B. Element transport from slab to volcanic front at the Mariana arc. *J. Geophys. Res.* **1997**, *102*, 14991–15018. [[CrossRef](#)]
59. Plank, T. *The Chemical Composition of Subducting Sediments*, 2nd ed.; Elsevier: Amsterdam, The Netherlands, 2013; Volume 4, ISBN 9780080983004.
60. Wegner, W.; Wörner, G.; Harmon, R.S.; Jicha, B.R. Magmatic history and evolution of the Central American Land Bridge in Panama since Cretaceous times. *Geol. Soc. Am. Bull.* **2011**, *123*, 703–724. [[CrossRef](#)]
61. Gualda, G.A.R.; Giorso, M.S.; Lemons, R.V.; Carley, T.L. Rhyolite-MELTS: A modified calibration of MELTS optimized for silica-rich, fluid-bearing magmatic systems. *J. Petrol.* **2012**, *53*, 875–890. [[CrossRef](#)]
62. Pearce, J.A.; Harris, N.B.W.; Tindle, A.G. Trace element discrimination diagrams for the tectonic interpretation of granitic rocks. *J. Petrol.* **1984**, *25*, 956–983. [[CrossRef](#)]



63. Wu, C.L.; Yao, S.Z.; Zeng, L.S.; Yang, J.; Wooden, J.; Chen, S.; Mazadab, F. Double subduction of the Early Paleozoic North Qilian oceanic plate: Evidence from granites in the central segment of North Qilian, NW China. *Geol. China* **2006**, *33*, 1197–1208.
64. Zhang, Y.; Li, X.; Pan, F.; Song, Z. LA-ICP-MS zircon U-Pb dating of the porphyaceous syenogranite in Niuxinshan along the central segment of North Qilian orogenic belt and its geological significance. *Geol. Bull. China* **2018**, *37*, 724–733.
65. Zhang, C.; Yu, X.; Yang, F.; Santosh, M.; Huo, D. Petrology and geochronology of the Yushigou nephrite jade from the North Qilian Orogen, NW China: Implications for subduction-related processes. *Lithos* **2021**, *380*, 105894. [[CrossRef](#)]
66. Liati, A.; Gebauer, D. Constraining the prograde and retrograde P-T-t path of Eocene HP rocks by SHRIMP dating of different zircon domains: Inferred rates of heating, burial, cooling and exhumation for central Rhodope, northern Greece. *Contrib. Miner. Pet.* **1999**, *135*, 340–354. [[CrossRef](#)]
67. Liu, Y.-X.; Wang, J.-R.; Liu, Y.-W.; Miao, X.-Q.; Chen, J.-L. Evolution of the Columbia supercontinent: Insights from the North Qilian Block, NW China. *Precambrian Res.* **2021**, *366*, 106424. [[CrossRef](#)]
68. Li, H.K.; Lu, S.N.; Xiang, Z.Q.; Zhou, H.Y.; Li, H.M.; Liu, D.Y.; Song, B.; Zheng, J.K.; Gu, Y. SHRIMP U-Pb geochronological research on detrital zircons from the Beidahe complex-group in the western segment of the North Qilian Mountains, Northwest China. *Geol. Rev.* **2007**, *53*, 132–140.
69. Calderon, M.; Prades, C.F.; Herve, F.; Avendaño, V.; Fanning, C.M.; Massonne, H.-J.; Theye, T.; Simonetti, A. Petrological vestiges of the Late Jurassic-Early Cretaceous transition from rift to back-arc basin in southernmost Chile: New age and geochemical data from the Capitán Aracena, Carlos III, and Tortuga ophiolitic complexes. *Geochem. J.* **2013**, *47*, 201–217. [[CrossRef](#)]
70. Saunders, A.D.; Tarney, J.; Stern, C.R.; Dalziel, I.W.D. Geochemistry of Mesozoic marginal basin floor igneous rocks from southern Chile. *Geol. Soc. Am. Bull.* **1979**, *90*, 237–258. [[CrossRef](#)]
71. Godard, M.; Bosch, D.; Einaudi, F. A MORB source for low-Ti magmatism in the Semail ophiolite. *Chem. Geol.* **2006**, *234*, 58–78. [[CrossRef](#)]
72. MacLeod, C.J.; Johan Lissenberg, C.; Bibby, L.E. “Moist MORB” axial magmatism in the Oman ophiolite: The evidence against a mid-ocean ridge origin. *Geology* **2013**, *41*, 459–462. [[CrossRef](#)]
73. Stern, R.J.; Gerya, T. Subduction initiation in nature and models: A review. *Tectonophysics* **2018**, *746*, 173–198. [[CrossRef](#)]
74. Zhou, X.; Li, Z.-H.; Gerya, T.V.; Stern, R.J.; Xu, Z.; Zhang, J. Subduction initiation dynamics along a transform fault control trench curvature and ophiolite ages. *Geology* **2018**, *46*, 607–610. [[CrossRef](#)]